HHS Public Access

Author manuscript

Mol Cancer Res. Author manuscript; available in PMC 2020 December 01.

Published in final edited form as:

Mol Cancer Res. 2020 June ; 18(6): 891–902. doi:10.1158/1541-7786.MCR-19-1208.

Kinetics of nuclear uptake and site-specific DNA cleavage during CRISPR-directed gene editing in solid tumor cells

Kelly Banas[1,2], **Natalia Rivera-Torres**[1], **Pawel Bialk**[1], **Byung-Chun Yoo**[1], **Eric B. Kmiec**[1,2,3]

[1]Gene Editing Institute, Helen F. Graham Cancer Center & Research Institute, ChristianaCare, 4701 Ogletown-Stanton Road, Suite 4300, Newark, Delaware 19713, (o) 302-623-0628

[2]Department of Medical and Molecular Sciences, University of Delaware, Willard E. Hall Education Building, Newark, Delaware 19716

Abstract

Clustered Regularly Interspaced Short Palindromic Repeats (CRISPR)-directed gene editing is approaching clinical implementation in cancer. Thus, it is imperative to define the molecular framework upon which safe and efficacious therapeutic strategies can be built. Two important reaction parameters include the biological time frame within which the CRISPR/Cas complex enters the nucleus and executes gene editing, and the method of discrimination that the CRISPR/Cas complex utilizes to target tumor cell, but not normal cell, genomes. We are developing CRISPR-directed gene editing for the treatment of non-small cell lung carcinoma (NSCLC) focusing on disabling Nuclear Factor Erythroid 2-Related Factor-Like (*NRF2*), a transcription factor that regulates chemoresistance and whose genetic disruption would enhance chemosensitivity. In this report, we define the time frame of cellular events that surround the initialization of CRISPR-directed gene editing as a function of the nuclear penetration and the execution of *NRF2* gene disruption. We also identify a unique protospacer adjacent motif (PAM) that facilitates site-specific cleavage of the *NRF2* gene present only in tumor genomes.

Introduction

Lung cancer is the leading cause of cancer-related death worldwide and accounts for an estimated 1.8 million newly diagnosed cases each year (1). Non-small-cell lung carcinoma (NSCLC) makes up 85% of lung cancer cases and is further subtyped as adenocarcinoma, squamous cell carcinoma and large-cell carcinoma. The five-year survival rate is 18% despite advances in prevention, screening and treatment (2). This high mortality rate is multifactorial, however, late stage diagnosis as well as resistance to treatment seem to have the most influence on poor patient outcomes. The first-line treatment for advanced or metastatic NSCLC includes platinum-based chemotherapy regimens and combinations with

[3]Corresponding author: Eric.B.Kmiec@Christianacare.org.

Dedication. This manuscript is dedicated to the Lung Cancer Working Group from the Helen F. Graham Cancer Center and Research Institute that was established in 2017 to help formulate the molecular basis of CRISPR-directed gene editing in solid tumors. This group includes Drs. Nicholas J. Petrelli, Greg Masters, Michael Guarino, Christopher Koprowski, Jamil Katri, Jerry Castellano and Ms. Pat Swanson.

The authors declare no potential conflicts of interest.

taxanes, as well as immunotherapy. Despite the various chemotherapy combinations available, a patient may become resistant to treatment and require two or three more lines of therapy (3,4).

From a clinical perspective, the well-known toxicity of chemotherapy often remains a serious barrier to successful treatment and even enrollment in clinical trials (5–7). Even though CAR T-cell therapy is considered a breakthrough for many cancer types, the cost, the recently identified self-immunity and even potential for bio-therapeutic toxicity remains an impediment for widespread implementation (8–10). Currently, CAR T-cell therapy is not an option for NSCLC, thus, there is an unmet medical need for the development of innovative approaches for the treatment of lung cancer.

New developments in precision medicine show tremendous promise for the development of novel, personal therapeutics (11). More recently, Clustered Regularly Interspaced Short Palindromic Repeats (CRISPR)-directed gene editing has already been approved for clinical trials by the USA FDA and similar organizations in Europe and China. While the field of gene editing in mammalian cells has been active for almost two decades, the focus of the early work centered on the mechanism of action and circuitry that regulates single-base repair (12). Thus, the scientific foundation of gene editing has been well established (13–15). However, with the emergence of CRISPR/Cas, gene editing became democratized when the bacterial system was reengineered to work in human cells (16–20). The standard paradigm, "*from bench to bedside",* has been accelerated because of the success and excitement that surrounds this technology. It is important to recognize that CRISPR-based therapeutic approaches have yet to be shown to be fully safe and lacking significant toxicity. Studies addressing these two key hurdles are now being carried out in both preclinical and phase 1/2 clinical trials. The Brilliance and the CTX001 clinical trial (21,22) are among some of the current investigations that should yield important results.

We have begun to investigate the feasibility of using CRISPR-directed gene editing in combination with standard of care for the treatment of solid tumors, including NSCLC. We have taken a decidedly reductionist approach wherein we created a CRISPR/Cas9 gene editing tool to disable the Nuclear Factor Erythroid 2-Related Factor-Like (*NRF2*) gene. NRF2 is a master regulator of 100–200 target genes involved in cellular responses to oxidative/electrophilic stress (23,24). NRF2 is also known to regulate the expression of genes involved in protein degradation and detoxification and is negatively regulated by Kelch-like ECH-associated protein 1 (KEAP1), a substrate adapter for the Cul3-dependent E3 ubiquitin ligase complex. Relevant to our overall objective, NRF2 expression increases significantly when a NSCLC patient is treated with chemotherapy, through an activation of target genes that trigger the cyto-protective response (25–27). Several studies have demonstrated that increased NRF2 expression is one of the major contributing factors of chemo-resistance in cancer cells, being more prevalent in NSCLC (24,28–30).

Previously, we discovered that successful functional knockout of the *NRF2* gene in chemo-resistant lung cancer cells significantly increased the anticancer activity of cisplatin, carboplatin and vinorelbine in both cell culture and mouse models (31). Our results prompted further exploration of the feasibility of innovative therapeutic approaches aimed at

reducing the clinical side effects of chemotherapy (11). This strategy centers on a combinatorial approach in which gene editing would disable the *NRF2* gene removing its global regulation of chemoresistance.

While CRISPR has already advanced into the clinical arena, fundamental molecular questions surrounding mode of action remain unanswered. First, is there a timeframe correlation between the timing of nuclear penetration and the emergence of CRISPR-directed mutagenesis? And, second, is there enough sequence divergence between normal and tumor cell genomes so that CRISPR complexes can selectively cleave and disrupt the *NRF2* gene in the tumor cell?

Regarding the first question, recent data suggest that a time lag exists between nuclear penetration and the appearance of gene editing activity in human cells (32). Therefore, we carried out a series of experiments to elucidate important reaction parameters that surround the coupling of nuclear penetration and gene editing activity. Our results indicate that the localization of the exogenously added CRISPR/Cas complex into the nucleus of the lung tumor cell is efficient and rapid; however, *NRF2* gene disruption lags significantly, seen after about eight hours as the gene editing components are visualized exiting the nucleus. With this data, we are able to create a snapshot of the time-course and processing of CRISPR/Cas in a lung cancer cell.

Regarding the second question, Kerins and Ooi (33) catalogued somatic *NRF2* mutations in various cancer cases reported in The Cancer Genome Atlas. They reported 214 cases of *NRF2* mutations, predominately found within the Neh2 domain or known as the KEAP1 binding domain of the protein. These mutations disrupt KEAP1 binding and lead to constitutive expression of NRF2 in cancer cells. The most common *NRF2* mutation noted, R34G, is of special interest because this mutation creates a new protospacer adjacent motif (PAM) for Cas9 recognition. The PAM consists of 2–6 nucleotides juxtaposed to the CRISPR seed binding sequence facilitating alignment and cleavage of the DNA. After cleavage, Cas9 creates blunt-end, double-stranded breaks which are then repaired by one of two mechanisms: non-homologous end joining (NHEJ) or homology-directed repair (HDR). NHEJ is responsible for insertions or deletions (indel) at the cut site, generating genetic knockouts (KO) of the gene and potentially causing loss of protein expression. HDR is the mechanism by which genes can be repaired using gene editing if an appropriate donor DNA template is provided. We provide evidence that a unique PAM site regulates selective cleavage of a tumor cell genome, establishing a foundational basis for CRISPR-directed gene editing in lung cancer.

MATERIALS AND METHODS

Cell Line and Culture Conditions

Human lung adenocarcinoma A549 cells (#CCL-185, passage number 1–12) and Human lung squamous cell carcinoma NCI-H1703 [H1703] cells (#CRL-5889, passage number 1–12) were purchased from ATCC (Manassas, VA, USA). Cells were thawed, according to the manufacturer's protocol. A549 cells were grown in F-12K medium (ATCC) supplemented with 10% fetal bovine serum (FBS) (ATCC) and 1% Penicillin-Streptomycin Solution

(ATCC). NCI-H1703 cells were grown in RPMI 1640 medium (ATCC) supplemented with 10% fetal bovine serum (FBS) (ATCC) and grown at 37°C in 5% CO_2. Both cell lines were tested for Mycoplasma upon thawing and before use in experiments using the MycoScope PCR Mycoplasma detection kit (Genlantis, Cat. MY01100). The A549 cell line was previously characterized by ATCC using Short Tandem Repeat (STR) profiling, cellular morphology and karyotyping. The H1703 cell line was previously characterized by ATCC using STR profiling and cellular morphology. No further authentication was performed.

CRISPR/Cas9 RNP Design and Assembly

Entrance and nuclear transit of the CRISPR/Cas complex—The *NRF2* gene-coding sequence was entered into Benchling (https://benchling.com) and the gRNA 5' TGGATTTGATTGACATACTT 3' within exon 2 was selected. The GFP-labeled SpCas9 protein was a kind gift from Integrated DNA Technologies. Unlabeled Alt-R SpCas9, Alt-R tracrRNA ATTO 550 and designed Alt-R crRNA were purchased from Integrated DNA Technologies. RNA oligos (crRNA and tracrRNA) were mixed in equimolar concentrations to a final duplex concentration of 20 μM, then annealed by heating the mix at 95 °C for 5 minutes and cooled to room temperature (15–25 °C). Prior to mixing with cells, crRNA:tracrRNA duplex (20 μM working solution) and spCas9 protein (62 μM stock solution) were mixed together for a final complexed concentration of 20 pmol and set to incubate at room temperature for 15 minutes.

Selective cleavage of a tumor genome specific PAM sequence—The *NRF2* gene-coding sequence was entered into Benchling (https://benchling.com) and the R34G mutation-specific gRNA 5'-GATATAGATCTTGGAGTAAG-3' and the nonspecific gRNA 5'-GTAACGGCAGACTTCTCCTC-3' (HBB RNP) were selected. Alt-R SpCas9, Alt-R tracrRNA and designed Alt-R crRNA were purchased from Integrated DNA Technologies and designed synthetic sgRNA was purchased from Synthego. RNA oligos (crRNA and tracrRNA) were mixed in equimolar concentrations to a final duplex concentration of 100 μM or 250 μM, then annealed by heating the mix at 95 °C for 5 minutes and cooled to room temperature (15–25 °C). Prior to mixing with cells, crRNA:tracrRNA duplex (100 μM or 250 μM) and spCas9 protein (100 μM or 50 μM) were mixed together and set to incubate at room temperature for 15 minutes. Final complexed concentrations were equimolar at 100 pmol or 5:1 ratio at 250:50 pmol of RNP.

Transfection Efficiency and Gene Editing Analysis

The Lonza SF Cell Line 4D-Nucleofector X Kit (Lonza Inc, Basel, Switzerland) was used for transfection of the RNP in the A549 and NCI-H1703 cell lines.

Entrance and nuclear transit of the CRISPR/Cas complex—For all experiments, A549 cells were seeded 48 hours prior to transfection and allowed to reach 60–80% confluency. On the day of transfection, A549 cells were harvested by trypsinization and washed twice with 1x PBS (−/−). Cells were resuspended at a concentration of 3×10^5 cells/20 μL in SF/supplement solution and 5 μL of 20 pmol labeled RNP complex was added for each sample. Lonza program CM-130 was used and after 15 minutes of rest, cells were transferred to a 6-well plate or a 1.5ml tube for further analysis.

A549 RNP fluorescence was measured by BD FACSAria II (BD Biosciences). Cells were harvested by trypsinization, washed three times and resuspended in 1x PBS (−/−) for FACS analysis. Several controls were used to establish gates based on each fluorescent component. The controls consisted of mock transfection of A549 cells, transfection of RNP with Cas9 (GFP), and transfection of RNP with tracrRNA (ATTO 550). Gates were established based on these parameters. After FACS analysis, cellular genomic DNA was isolated from each sample using the DNeasy Blood and Tissue Kit (Qiagen, Cat. 69506). The region surrounding the CRISPR target site was PCR amplified using Q5 High-Fidelity 2X Master Mix (New England BioLabs, Cat. M0492) (762 bp, forward primer 5'-CACCATCAACAGTGGCATAATGTGAA-3', reverse primer 5'-AACTCAGGTTAGGTACTGAACTCATCA-3'). The PCR reaction was purified using the QIAquick PCR Purification Kit (Qiagen, Cat. 28106) and sent out to GENEWIZ, LLC (South Plainfield, NJ) for Sanger Sequencing.

Selective cleavage of a tumor genome specific PAM sequence—A549 and NCI-H1703 cells were seeded 48 hours prior to transfection and allowed to reach 60–80% confluency. On the day of the transfection, cells were harvested by trypsinization and washed twice with 1x PBS (−/−). Cells were resuspended at a concentration of 3×10^5 cells/20 μL in SF/supplement solution and 5 μL of RNP complex was added to each sample. For transfection efficiency by FACS analysis, the pmaxGFP vector (0.2 μg) was added to the respective samples before transfection. Lonza program CM-130 was used and after 15 minutes of rest, cells were transferred to a 6-well plate for 48 hours.

Transfection efficiency of A549 and NCI-H1703 cells was measured by BD FACSAria II 48 hours after transfection. Cells were harvested by trypsinization, washed three times and resuspended in 1x PBS (−/−) for FACS analysis. After FACS analysis, cellular genomic DNA was isolated from each sample using the DNeasy Blood and Tissue Kit. The region surrounding the CRISPR target site was PCR amplified using Q5 High-Fidelity 2X Master Mix (530 bp, forward primer 5'-CACCATCAACAGTGGCATAATGTGAA-3', reverse primer 5'-AACTCAGGTTAGGTACTGAACTCATCA-3'). The PCR reaction was purified using the QIAquick PCR Purification Kit, Sanger sequenced using a SeqStudio Genetic Analyzer (Applied Biosystems) and analyzed by TIDE (34).

Western Blot Analysis

A549 cells were transfected with unlabeled Cas9 RNP as described above. Cells were harvested at the indicated time points and the western blot was carried out as previously described(31). Primary antibody incubation was performed overnight on a shaker at 4°C for Cas9 (1:5,000, Abcam ab210752), and GAPDH (1:10,000, Abcam ab8245), and secondary antibody (Jackson ImmunoResearch Laboratories, West Grove, PA, USA) incubations were all done 1 hr at room temperature at a 1:10,000 dilution. The protein bands were visualized via chemiluminescence using a SuperSignal West Dura Extended Duration ECL (Pierce) and detected on the LI-COR Odyssey FC.

Fluorescence Microscopy

Transfected A549 cells were seeded in 4-well chambers (LabTek II). Before imaging at each indicated time point, cells were washed twice with PBS (−/−) and incubated with Hoechst 33258 (1:10,000, Invitrogen, Cat. H3569) for a minimum of 15 minutes at room temperature in the dark. Chambers were imaged at 20x magnification using the DAPI (358 nm), GFP (488 nm), and DsRed (560 nm) channels on the Zeiss Axio fluorescent observer.Z1 microscope. Random fields were imaged and images were processed on the AxioVision software. The brightness and contrast of the images have been enhanced for better visualization.

CRISPR-Directed Mutagenesis

A *NRF2* gene expression plasmid (pcDNA3-EGFP-C4-NRF2) was purchased from Addgene. The plasmid was mutated using CRISPR-directed mutagenesis (CDM) as described by Sansbury et al (35). CDM was achieved using two Cas12a cleavage sites (crRNA: 5'-ATTGACATACTTTGGAGGCAA-3', 5'- GAGTTGTTCTTGTCTTTCCTT-3') and two oligonucleotides, containing the intended R34G mutation, (ssDNA: 5'-CAAGATATAGATCTTGGAGTAAGTGGAGAAGTATTTGAC

TTCAGTCAGCGACGGAAAGAGTATGAGCTGGAAAAACAGAAAAAACTTG-3', 5'-CTTTTCAAGTTTTTTCTGTTTTTCCAGCTCATACTCTTTCCGTCGCTGACTGAAGTC AAATACTTCTCCACTTACTCCAAGATCTATA-3') were annealed to create the template. Plasmids were amplified using Q5 High-Fidelity 2X Master Mix (901 bp, forward primer 5'-CATGGTCCTGCTGGAGTTCGTG-3', reverse primer 5'- GAGGATGCTGCTGAAGGA ATCCTC-3').

In vitro Cleavage Assay

A549 (parental and clonal) and NCI-H1703 cell lines were harvested and genomic DNA was isolated using the DNeasy Blood and Tissue Kit. *NRF2* exon 2 was amplified using Q5 High-Fidelity 2X Master Mix (530 bp, FWD 5'-CACCATCAACAGTGGCATAATGTGAA-3', REV 5'-AACTCAGGTTAGGTACTGAACTCATCA-3') and amplicons were purified using the QIAquick PCR Purification Kit. The gRNAs used for the *in vitro* cleavage assays were R34G gRNA (5'-GATATAGATCTTGGAGTAAG-3') and HBB gRNA (5'-GTAACGGCAGACTTCTCCTC-3').

RNP Assembly—RNA oligos (crRNA and tracrRNA) were mixed in equimolar concentrations to a final duplex concentration of 10 μM then annealed by heating the mixture at 95 °C for 5 minutes and cooled to room temperature (15–25 °C). The crRNA:tracrRNA duplex (10 μM) and spCas9 protein (100 μM) were complexed together in PBS (−/−) to a final concentration of 1 μM and incubated at room temperature for 10 minutes.

In vitro Digestion Reaction—The reaction was assembled using 10X NEBuffer 3.1 (New England BioLabs, cat.B7203S) (1X final concentration), 1 μM Cas9 RNP (molar concentrations were adjusted for each reaction), 100 ng DNA substrate, and nuclease-Free

water. The reaction was incubated at 37°C for 60 min. The reaction was stopped by adding 1 μL Proteinase K (20 mg/mL) to the mixture at 56°C for 10 min and visualized by gel electrophoresis.

Results

Entrance and nuclear transit of the CRISPR/Cas ribonucleoprotein complex in lung cancer cells

We sought to examine the temporal relationship among cellular penetration, nuclear transit and gene editing activity vis-à-vis indel formation on the clinically relevant gene *NRF2*. To do so, we developed a CRISPR-directed gene editing strategy to target within the Neh2 domain of the NRF2 protein, encoded by exon 2 (Figure 1A), using a dual fluorescently tagged CRISPR/Cas9 ribonucleoprotein (RNP) complex; the tracrRNA contained an ATTO 550 label and purified Cas9 protein was tagged with GFP (Figure 1B). After cell preparation and RNP assembly, A549 cells were transfected by Nucleofection with the dual labeled particle. After a designated period of time, we examined the targeted cell population by: 1) FACS for single and dual transfection efficiency of the ribonucleoprotein components (Figure 1C), 2) fluorescent microscopy to visualize cellular and nuclear uptake, 3) western blot analysis for the presence and sustainability of Cas9 protein, and 4) gene editing activity on the *NRF2* gene using Sanger sequencing and the Tracking of Indel DEcomposition (TIDE) program (34).

Fluorescence-Activated Cell Sorting (FACS) enables analyses of the transfection efficiency and cellular uptake through visualization of all four quadrants for co-localization of the ATTO 550 and GFP fluorescent tags respectively (Figure 2). The control data addressing compensation and gating position for FACS are shown in supplemental figure 1. The red area (P1) of each left-hand graph represents the collected cell population analyzed for fluorescence intensity, shown in the right-hand graph. The Y axis (FITC channel) represents GFP fluorescence intensity and the X axis (PE channel) represents ATTO 550 fluorescence intensity. Quadrant 1 (Q1) contains cells positive for only GFP (Cas9) while quadrant 2 (Q2) reflects cells containing both GFP and ATTO 550 (tracrRNA) fluorescence (outlined in green). Population 2 (P2), highlighted in green, was gated to capture GFP-positive cells that may have been omitted with standard gating (data not shown). Quadrant 3 (Q3) contains cells that do not exceed background fluorescence and quadrant 4 (Q4) contains cells positive for only ATTO 550 (tracrRNA). The table under each plot contains raw data from each quadrant. The fluorescence (%) found in quadrant 2 is of interest because this population represents cells that contain both fluorescent tags, presumably a co-localization of the two components of the RNP complex.

In each FACS plot of Figure 2, quadrant 1 reveals almost no GFP fluorescence indicating that Cas9 is likely complexed with tracrRNA after introduction into the cell. Supplemental data (Supplemental Figure 1) confirm that the Cas9 (GFP) molecule is detectable in cells in quadrant 1 when transfected in the absence of other fluorescent components. GFP-fluorescing cells slowly disappear from all quadrants over eight hours, indicating degradation through loss of signal. Similarly, ATTO 550-fluorescing cells are observed at high levels in quadrant 4 after one hour and gradually diminish over the next twenty-four to

forty-eight hours (see Supplemental Figure 1). After twelve hours, total fluorescence (the sum of quadrant 1, 2 and 4) declines precipitously (Figure 2) correlating with the images provided by fluorescent microscopy. Taken together, we are observing the decomposition of the CRISPR/Cas9 complex over time, with Cas9 disappearing first followed by the tracrRNA.

In correlation with the FACS time course, we carried out gene editing analysis at the same time points. Exon 2 was amplified, Sanger sequenced and analyzed by TIDE to quantify indel formation within the total, unsorted population (Figure 3). Indel formation appears to rise slowly, but steadily, throughout the course of the reaction with significant levels visible only after 8 hours, coincident with the increase in fluorescent signal of quadrant 4 of the FACS plots (Figure 2).

Next, we imaged nuclear entry, co-localization and exit of the RNP components by fluorescent microscopy (Figure 4A). Cells were stained with Hoechst 33258 to visualize the nucleus using the DAPI channel while fluorescent CRISPR complex components were visualized using GFP and DsRed channels respectively. Brightness and contrast of the images are enhanced for better visualization of the fluorescent RNP components (see also Supplemental Figure 2). The tracrRNA (ATTO 550) localizes rapidly into the nucleus while Cas9 (GFP) appears punctate at the nuclear membrane, merging or coalescing into the nucleus after four hours. Between one and eight hours, tracrRNA (ATTO 550) fluorescence appears throughout the nucleus and cytoplasm, and after eight hours, both Cas9 and tracrRNA appear to exit the cell. At twenty-four hours, Cas9 (GFP) is barely visible apart from the punctate remnants surrounding the nucleus and only small traces of tracrRNA (ATTO 550) remain visible in the nucleus. After forty-eight hours, both fluorescent components are barely detectable even with enhancement.

In Figure 4B, we present a graphical representation of the individual and dual fluorescence obtained from FACS analysis. Combining FACS analyses and indel formation data, the reaction could be generally broken down into two phases. Phase I encompasses RNP delivery and nuclear uptake along with the initial signals of CRISPR-directed DNA cleavage and indel formation through NHEJ of a single target site; phase II reveals elevated levels of indel formation likely through resection and repair of the target site after cleavage, and the exit of the two fluorescent RNP components from the cell. Figure 4C represents Cas9 protein at each time point through Western blot analysis using an antibody directed against SpCas9. In our hands, the majority of Cas9 protein appears in the first four hours after introduction into the cell and becomes undetectable somewhere between four and eight hours after transfection.

The total number of cells with both fluorescent signals in quadrant 2 is seen to decrease over time with the maximal level observed at one-hour post nucleofection; a significant drop is seen between four and eight hours. The totality of fluorescent cells in quadrant 2 and quadrant 4 remain consistent throughout most of the reaction time (until twelve hours) indicating that the cells receiving the RNP gradually lose GFP fluorescence first, while retaining ATTO 550 fluorescence for a longer period. These results suggest both labels are inside the targeted cell population for approximately one to four hours. The presence of

intact Cas9 protein in the cell, as viewed by western blot, confirms this time frame (see Figure 4C).

Selective cleavage of a tumor genome specific PAM sequence by CRISPR/Cas9

A second question to support the concept of using CRISPR-directed gene editing for lung cancer centers on the selective activity of programmable nucleases on tumor cell genomes, avoiding similar activity on normal cell genomes. Due to the mechanism of CRISPR/Cas cleavage, a PAM sequence is required and can be selected through copious design of the crRNA seed sequence. As described above, tumor cell-specific sequence variance has already been identified in several lung cancer genomes. The R34G mutation was initially found because it inhibits KEAP1-mediated degradation of NRF2 which in turn, causes increased NRF2 stability and nuclear accumulation (33,36). This mutation occurs as a result of a base change from cytosine to guanine in the first base of codon 34 in *NRF2*, thereby creating a unique Cas9 PAM site (Figure 5A).

As proof of concept, the following experiments were conducted to assess the level of discrimination and selectivity of the R34G mutation-specific CRISPR/Cas9 complex. An *in vitro* cleavage assay was employed to assess the discriminatory cleavage activities of this CRISPR/Cas complex. The RNP was incubated with varying DNA templates and the cleavage products were visualized by gel electrophoresis. For this experiment, wildtype and R34G-mutated *NRF2* PCR products (901 bp) from an *NRF2* expression plasmid (Figure 5B) were incubated with R34G-specific RNP (1 μM). Cleavage products were visualized by gel electrophoresis and the results are shown in Figure 5C. A nonspecific RNP (*HBB* RNP) was also used to confirm specificity and selectivity of the new PAM site. In lane 6 (R34G NRF2 – R34G RNP), two new bands (222 & 679 bp) appear and are the result of tumor genome specific RNP cleavage; the R34G-targeting RNP only recognizes and cleaves the mutated DNA sequence.

To assess specificity and fidelity of the R34G-mutation specific RNP in lung tumor cells, we use the well-established non-small-cell lung adenocarcinoma cell line A549 because it is often used as a gold standard for the discovery of anti-cancer therapeutics. We genetically engineered the A549 cell line to contain the R34G mutation in exon 2 of the *NRF2* gene using previously established methods (37). A secondary cell line derived from a lung squamous cell carcinoma, NCI-H1703, was also selected to ensure reproducibility of the cell-based experiments. The parental A549 cell line, R34G-mutated A549 cell line (A549 R34G-6) and NCI-H1703 cell line were sequenced across exon 2 to verify the sequence of the Neh2 domain. Both A549 and NCI-H1703 parental cell lines contain no mutations within exon 2 of the *NRF2* gene, whereas, the A549 R34G-6 cell line contains a heterozygous R34G mutation (Figure 6A). The A549 cell line is known to be bi– and tri-allelic, therefore, the R34G mutation in the A549 R34G-6 clone is believed to be on two of three alleles as seen by the double peak of the ‘G’ nucleotide (black peak) as compared to the peak of the ‘C’ nucleotide (blue peak), indicated by the red arrow under ‘A549 R34G-6’ (Figure 6A).

Genomic DNA from each cell line was used to amplify exon 2 of the *NRF2* gene. The PCR products (530 bp) were then used in *in vitro* cleavage reactions where expected cleavage

products would appear at 385 and 145 bp and uncut product would appear at 530 bp, indicated by the red lines along the ladder (Figure 6B). The R34G-targeting RNP was used at two concentrations (1 & 5 pmol) with each sample (lanes 2, 3, 5, 6, 8, 9). Minimal cleavage is seen with wildtype *NRF2* sequence in the A549 and NCI-H1703 parental cell lines (lanes 3 & 6), whereas cleavage products (145 & 385 bp) are abundantly clear in the A549 R34G-6 cell line with the R34G-mutated *NRF2* sequence (lanes 8 & 9). These data further confirm the specificity and efficacy of the R34G-targeting RNP, only recognizing the target DNA in the presence of the R34G mutation in exon 2 of *NRF2*. Minor residual cleavage of the wildtype *NRF2* sequence can be explained by the nature of the cleavage reaction and sequence homology of the guide RNA to the target DNA as the cleavage reaction includes incubating target DNA with RNP for an hour. Cleavage specificity is further confirmed through dose dependent cleavage reactions with a minimum of half the standard concentration and a maximum of five times the standard concentration of RNP. The range of concentrations do not result in cleavage of wildtype *NRF2* sequence whereas with a R34G-mutated *NRF2* sequence, cleavage products can be seen even with half of the standard concentration of the R34G-targeting RNP (Supplemental Figure 3).

Finally, we evaluated selective CRISPR-directed gene editing at the *NRF2* locus and measured indel formation in three separate cell lines (A549 parental, A549 R34G-6, NCI-H1703 parental), each of which are predicted to produce a different outcome. Figure 7 depicts the genetic analysis of each cell line after transfection of the R34G-targeting RNP under three different conditions: 1) equimolar concentration of duplexed guide RNA to Cas9 (top panel); 2) five times the amount of duplexed guide RNA to Cas9 (middle panel); 3) five times the amount of single guide RNA to Cas9 (bottom panel). The pMAX GFP vector, supplied by Lonza, was used as a control for transfection efficiency. TIDE analysis was employed to determine total indel formation efficiency. Wildtype or uncut sequences appear at the 0 tick mark as a pink bar and would indicate alleles unaffected by the cleavage activity of the R34G-specific RNP.

Figure 7A depicts the genetic analysis after transfection of the R34G-targeting RNP in the A549 parental cells. The A549 parental cells contain a wildtype *NRF2* gene therefore there is no native CRISPR/Cas9 recognition site for the R34G-targeting RNP. Genomic DNA from the transfected cells was analyzed by TIDE analyses (shown in Figure 7A). The top panel displays indel efficiency and sequence alignment of an unsorted population. According to TIDE analysis, there is a total indel efficiency of 11.8% and statistically insignificant insertions and deletions (black bars – p value > 0.001). The middle panel shows a total indel efficiency of 4.3% from a GFP-positive sorted population with only statistically insignificant insertions or deletions. The bottom panel shows a total indel efficiency of 11.4% from a GFP-positive sorted population with one statistically significant insertion (+1 bp).

Figure 7B depicts the genetic analysis after transfection of the R34G-targeting RNP in the A549 R34G-mutated clonal cell line (A549 R34G-6). The A549 R34G-6 cells contain a heterozygous R34G mutation in exon 2 of the *NRF2* gene, creating a new CRISPR/Cas9 recognition site for the R34G-targeting RNP. Genomic DNA from transfected cells was analyzed for gene editing activity by TIDE analyses (shown in Figure 7B). The top panel

shows indel efficiency and sequence alignment of an unsorted population with a total indel efficiency of 43.0% and statistically significant insertions (+1, 30 bp) and deletions (−9, 41 bp) along with several insignificant deletions. The middle panel shows a total indel efficiency of 55.7% from a GFP-positive sorted population with statistically significant insertions (+1, 30 bp) and deletions (−1, 9 bp) and insignificant deletions. The bottom panel shows a total indel efficiency of 32.7% with significant insertions (+1, 30 bp) and deletions (−2 bp) and insignificant indels from a GFP-positive sorted population. The lower R^2 value indicates some of the sequence analysis is unaccounted for likely because of sequence quality.

Figure 7C depicts the genetic analysis after transfection of the R34G-targeting RNP in the NCI-H1703 cell line, which contains a wildtype *NRF2* gene and no native CRISPR recognition site. Genomic DNA from transfected cells was analyzed for gene editing activity by TIDE analyses (shown in Figure 7C). The top panel shows total indel efficiency of 0.0% from an unsorted population. The bottom panel shows total indel efficiency of 4.6% with only insignificant indels from a GFP-sorted population.

Taken together, these data confirm the highly specific activity of the R34G RNP in the presence of the R34G mutation. We can infer that the R34G mutation does in fact create a new CRISPR/Cas9 recognition site that is actively cleaved when tested *in vivo*. The R34G-targeting RNP differentiates between the wildtype and R34G-mutated *NRF2* alleles within the A549 R34G-6 clonal cell line. This is seen by the remaining wildtype sequence (displayed at the 0-tick mark) in each panel of Figure 7B, which approximately equates to the percentage of wildtype NRF2 allele present in the cells.

Discussion

Clinical translation of CRISPR-directed gene editing is occurring at an unprecedented pace and there is great hope for therapeutic breakthroughs (38,39). And, while the technology appears to be democratized, there are several important questions that need to be addressed to ensure safety and success. We have taken a decidedly reductionist approach centering on some foundational molecular interactions that likely regulate the gene editing process. First, we begin to define the time required for CRISPR/Cas complexes to enter the cell, localize in the nucleus and execute gene disruption. Second, we evaluate a new experimental strategy wherein CRISPR/Cas is designed to catalyze cleavage selectively on tumor cell genomes. This parameter is at the heart of the conundrum that has faced gene therapy applications in general: can a specific genetic disruption be made solely in tumor cell genomes while leaving the normal cell genomes genetically unaltered? While we are establishing a molecular foundation for CRISPR-directed gene editing for future clinical application, safety, control of expression in non-tumor tissue and a thorough evaluation of preclinical response data must be clearly addressed.

We analyzed the efficiency of cellular transfection of an RNP particle bearing differential fluorescent labels and assessed the emergence of indels. We imaged the nuclear transit and positioning of the tracrRNA and Cas9 as a complex as they relate to the timing of indel formation. Our results indicate that gene editing of the *NRF2* gene in A549 cells may take

place in two experimentally segmented phases. Cas9 levels diminish significantly between four and eight hours correlating with their exit from the nucleus. In contrast, the fluorescently labeled tracrRNA transits into the nucleus rapidly and remains visible for up to eight hours. Both fluorescent labels evolve as punctate particles on the nuclear membrane at twelve hours prior to being diluted and rendered undetectable between twenty-four and forty-eight hours.

The initialization of genetic disruption through gene editing begins with a CRISPR/Cas complex aligning in homologous register with a target gene, facilitating site-specific double-stranded DNA breakage (40–43). Double stranded DNA breaks are most often repaired through a process known as Non-Homologous End Joining (NHEJ), an imperfect and unfaithful process in which nucleotides are lost or gained, generating functional knockouts. Contrasting data centered around the question of how long it takes for double-strand breaks to be created and repaired has been published with bulk measurements consistently showing that double-strand breaks have a half-life of ten to sixty minutes (32,44–46). However, these measurements lack the sensitivity that is required to follow double-strand breaks occurring and being repaired at a single locus, the reaction mechanics of CRISPR/Cas9. A crude estimate from Kim et al (47) suggested that indel formation by CRISPR/Cas occurs early in the process but is detected only after about fifteen hours. These data align with the belief that sequence specific nucleases direct indel formation only after multiple cycles of breakage and perfect repair (32). Our data suggest that the time delay between nuclear localization and detectable gene editing activity centers around four to eight hours (48).

Multiple pathways contribute to the repair of a Cas9 induced double-strand break (49) and relative activity of each is dependent on the locus, the metabolic state of the cell, and the half-life of the bound CRISPR complex. Indel formation likely emerges after multiple rounds of cleavage and repair once the cell has extinguished its energy supply which then causes error-prone repair of the double-strand breaks. It is possible that NHEJ initially prevents access of the Microhomology-mediated End Joining (MMEJ) pathway proteins to the double-strand break. Only after several hours wherein nonhomologous end joining has failed to repair the break, does the MMEJ pathway engage. We detect gene editing activity several hours after the RNP particle has successfully been transduced to the nucleus, a timeframe that aligns with the reaction mechanics of NHEJ and MMEJ. Our data suggest an inverse relationship among important steps in the gene editing reaction: cellular uptake, nuclear localization of multiple components, indel formation and particle and/or component exit.

We also evaluated a strategy that exploits a DNA change that creates a unique PAM site in the *NRF2* gene. A *NRF2* gene expression plasmid was used as a template to generate PCR products that we showed were specifically and uniquely cleaved by the R34G RNP, in the presence of the R34G mutation. We followed up with a series of experiments, that utilized a genetically modified cell line containing the R34G mutation as a new PAM site to create an *in vivo* PCR product that was subsequently cleaved again specifically by the R34G RNP. Finally, we targeted several cell lines directly using the R34G RNP and showed by TIDE analysis that efficient and highly specific indel formation is observed in a cell line that bears the R34G PAM site. Thus, by multiple iterations of the same basic experiment, we conclude

that the R34G RNP demonstrates a high level of specificity of *NRF2* gene disruption in an efficacious and efficient fashion. We believe that we have begun to establish a foundational basis for moving such a strategy forward to more complex targets in Xenograft mouse models.

NRF2 mutations occur in about 15% of lung squamous cell carcinomas, among other common cancer types (33). Disrupted NRF2 protein accumulates in the cytoplasm and nucleus, causing these cells to become resistant to toxic insults such as platinum-based drugs or radiation. Ultimately, this allows the cells to continue to grow and proliferate regardless of the environment. Despite the prevalence of mutations and the dismal prognosis of patients with elevated *NRF2* expression, there is no targeted therapy. Clinically, we envision a unique approach to target *NRF2* mutations using the gene editing tool, CRISPR/Cas9. This approach would also minimize the risk of off target effects and improve delivery method. These mutations have been noted in other cancer types as well which makes this approach a platform therapy.

The CRISPR-directed gene editing strategy could evolve as an effective augmentative therapy to approach patients with locally advanced lung cancer, especially where the current standard of care has failed and there may be resistance to standard chemotherapy. We recognize that enhancing sensitivity to chemotherapy in such patients could only provide an improvement in the quality of life for a limited amount of time. However, in some cases, current and alternative therapies are employed often to achieve the same end point (50). As such, we remain realistic and only cautiously optimistic. Ultimately, if this proves to be an effective strategy, it could be incorporated into an earlier stage including those patients treated adjunctively following surgical resection, or concurrently in combination with radiotherapy. By destroying the *NRF2* gene in a tumor cell population, the source of chemo-resistant cells is immaterial, since CRISPR-directed gene editing is active on tumor cells regardless of origin. A differential PAM site exists in tumors from esophageal, head and neck, uterine-endometrial and bladder-urothelial cancers which might provide a path to exploit tumor cell sequence variance as a method of selection.

Supplementary Material

Refer to Web version on PubMed Central for supplementary material.

Acknowledgments

We thank the members of the Kmiec laboratory for input and advice. We thank Dr. Lynn Opdenaker at the CTCR Flow Cytometry Core Facility for running, analyzing, and sorting cells. This project was supported by the Delaware INBRE and COBRE programs, with grants from the National Institute of General Medical Sciences – P20 GM103446 and P20 GM109021 from the State of Delaware. This content is solely the responsibility of the authors and does not necessarily represent the official views of the NIH.

REFERENCES

1. Gridelli C et al. Non-small-cell lung cancer. Nat. Rev. Dis. Prim 1, 15009 (2015). [PubMed: 27188576]
2. Siegel RL, Miller KD & Jemal A Cancer statistics, 2018. CA. Cancer J. Clin 68, 7–30 (2018). [PubMed: 29313949]

3. Chang A Chemotherapy, chemoresistance and the changing treatment landscape for NSCLC. Lung Cancer 71, 3–10 (2010). [PubMed: 20951465]
4. Wang H, Li M, Rinehart JJ & Zhang R Pretreatment with dexamethasone increases antitumor activity of carboplatin and gemcitabine in mice bearing human cancer xenografts: in vivo activity, pharmacokinetics, and clinical implications for cancer chemotherapy. Clin. Cancer Res 10, 1633–44 (2004). [PubMed: 15014014]
5. Pirker R et al. Cetuximab plus chemotherapy in patients with advanced non-small-cell lung cancer (FLEX): an open-label randomised phase III trial. Lancet 373, 1525–1531 (2009). [PubMed: 19410716]
6. Reck M et al. Phase III Trial of Cisplatin Plus Gemcitabine With Either Placebo or Bevacizumab As First-Line Therapy for Nonsquamous Non–Small-Cell Lung Cancer: AVAiL. J. Clin. Oncol 27, 1227–1234 (2009). [PubMed: 19188680]
7. Maemondo M et al. Gefitinib or Chemotherapy for Non–Small-Cell Lung Cancer with Mutated EGFR. N. Engl. J. Med 362, 2380–2388 (2010). [PubMed: 20573926]
8. Sun S, Hao H, Yang G, Zhang Y & Fu Y Immunotherapy with CAR-modified T cells: Toxicities and overcoming strategies. J. Immunol. Res 2018, (2018).
9. Srivastava S & Riddell SR Chimeric Antigen Receptor T Cell Therapy: Challenges to Bench-to-Bedside Efficacy. J. Immunol 200, 459–468 (2018). [PubMed: 29311388]
10. Shah NN & Fry TJ Mechanisms of resistance to CAR T cell therapy. Nat. Rev. Clin. Oncol 16, 372–385 (2019). [PubMed: 30837712]
11. Hirsch FR, Suda K, Wiens J & Bunn PA New and emerging targeted treatments in advanced non-small-cell lung cancer. Lancet 388, 1012–1024 (2016). [PubMed: 27598681]
12. Woolf TM, Gurumurthy CB, Boyce F & Kmiec EB To cleave or not to cleave: Therapeutic gene editing with and without programmable nucleases. Nat. Rev. Drug Discov 16, 296 (2017). [PubMed: 28303022]
13. Guha TK, Wai A & Hausner G Programmable Genome Editing Tools and their Regulation for Efficient Genome Engineering. Comput. Struct. Biotechnol. J 15, 146–160 (2017). [PubMed: 28179977]
14. Kim H & Kim J-S A guide to genome engineering with programmable nucleases. Nat. Rev. Genet 15, 321–334 (2014). [PubMed: 24690881]
15. Gaj T, Gersbach CA & Barbas CF ZFN, TALEN, and CRISPR/Cas-based methods for genome engineering. Trends Biotechnol. 31, 397–405 (2013). [PubMed: 23664777]
16. Doudna JA & Charpentier E The new frontier of genome engineering with CRISPR-Cas9. Science (80-.). 346, (2014).
17. Hsu PD, Lander ES & Zhang F Development and applications of CRISPR-Cas9 for genome engineering. Cell 157, 1262–78 (2014). [PubMed: 24906146]
18. Komor AC, Badran AH & Liu DR CRISPR-Based Technologies for the Manipulation of Eukaryotic Genomes. Cell 168, 20–36 (2017). [PubMed: 27866654]
19. Staahl BT et al. Efficient genome editing in the mouse brain by local delivery of engineered Cas9 ribonucleoprotein complexes. Nat. Biotechnol 35, 431–434 (2017). [PubMed: 28191903]
20. Zetsche B et al. Cpf1 Is a Single RNA-Guided Endonuclease of a Class 2 CRISPR-Cas System. Cell 163, 759–771 (2015). [PubMed: 26422227]
21. Single Ascending Dose Study in Participants With LCA10. Clinicaltrials.gov (2019). at <https://clinicaltrials.gov/ct2/show/NCT03872479 (Identifier: NCT03872479)>
22. A Safety and Efficacy Study Evaluating CTX001 in Subjects With Severe Sickle Cell Disease. Clinicaltrials.gov (2018). at <https://clinicaltrials.gov/ct2/show/NCT03745287?term=crispr&draw=2 (Identifier: NCT03655678)>
23. Chen J, Solomides C, Simpkins F & Simpkins H The role of Nrf2 and ATF2 in resistance to platinum-based chemotherapy. Cancer Chemother. Pharmacol 79, 369–380 (2017). [PubMed: 28120035]
24. Wang X-J et al. Nrf2 enhances resistance of cancer cells to chemotherapeutic drugs, the dark side of Nrf2. Carcinogenesis 29, 1235–43 (2008). [PubMed: 18413364]

25. Teppo H-R, Soini Y & Karihtala P Reactive Oxygen Species-Mediated Mechanisms of Action of Targeted Cancer Therapy. Oxid. Med. Cell. Longev 2017, 1485283 (2017). [PubMed: 28698765]
26. Rojo de la Vega M, Chapman E & Zhang DD NRF2 and the Hallmarks of Cancer. Cancer Cell 34, 21–43 (2018). [PubMed: 29731393]
27. Yang H et al. The role of cellular reactive oxygen species in cancer chemotherapy. J. Exp. Clin. Cancer Res 37, (2018).
28. Frank R et al. Clinical and Pathological Characteristics of KEAP1- and NFE2L2-Mutated Non-Small Cell Lung Carcinoma (NSCLC). Clin. Cancer Res 24, 3087–3096 (2018). [PubMed: 29615460]
29. Singh A et al. Dysfunctional KEAP1-NRF2 interaction in non-small-cell lung cancer. PLoS Med. 3, e420 (2006). [PubMed: 17020408]
30. Tian Y et al. Modification of platinum sensitivity by KEAP1/NRF2 signals in non-small cell lung cancer. J. Hematol. Oncol 9, 83 (2016). [PubMed: 27601007]
31. Bialk P, Wang Y, Banas K & Kmiec EB Functional Gene Knockout of NRF2 Increases Chemosensitivity of Human Lung Cancer A549 Cells in Vitro and in a Xenograft Mouse Model. Mol. Ther. - Oncolytics 11, 75–89 (2018). [PubMed: 30505938]
32. Brinkman EK et al. Kinetics and Fidelity of the Repair of Cas9-Induced Double-Strand DNA Breaks. Mol. Cell 70, 801–813.e6 (2018). [PubMed: 29804829]
33. Kerins MJ & Ooi A A catalogue of somatic NRF2 gain-of-function mutations in cancer. Sci. Rep 8, 12846 (2018). [PubMed: 30150714]
34. Brinkman EK, Chen T, Amendola M & van Steensel B Easy quantitative assessment of genome editing by sequence trace decomposition. Nucleic Acids Res. 42, e168–- (2014). [PubMed: 25300484]
35. Sansbury BM et al. CRISPR-Directed Gene Editing Catalyzes Precise Gene Segment Replacement In Vitro Enabling a Novel Method for Multiplex Site-Directed Mutagenesis. Cris. J 2, 121–132 (2019).
36. Fabrizio FP, Sparaneo A, Trombetta D & Muscarella LA Epigenetic versus Genetic Deregulation of the KEAP1/NRF2 Axis in Solid Tumors: Focus on Methylation and Noncoding RNAs. Oxid. Med. Cell. Longev 2018, 1–21 (2018).
37. Rivera-Torres N, Banas K, Bialk P, Bloh KM & Kmiec EB Insertional Mutagenesis by CRISPR/Cas9 Ribonucleoprotein Gene Editing in Cells Targeted for Point Mutation Repair Directed by Short Single-Stranded DNA Oligonucleotides. PLoS One 12, e0169350 (2017). [PubMed: 28052104]
38. Begley S & Feuerstein A First CRISPR treatment for blood diseases shows early benefits. Stat (2019). at <https://www.statnews.com/2019/11/19/first-crispr-treatment-for-blood-diseases-shows-early-benefits/>
39. First CRISPR study inside the body to start in U.S. Stat (2019). at <https://www.statnews.com/2019/07/25/first-crispr-study-inside-body-starting/>
40. Barrangou R & Doudna JA Applications of CRISPR technologies in research and beyond. Nat. Biotechnol 34, 933–941 (2016). [PubMed: 27606440]
41. Prakash V, Moore M & Yáñez-Muñoz RJ Current Progress in Therapeutic Gene Editing for Monogenic Diseases. Mol. Ther 24, 465 (2016). [PubMed: 26765770]
42. Carroll D Genome editing: progress and challenges for medical applications. Genome Med. 8, 120 (2016). [PubMed: 27846896]
43. Jinek M et al. A Programmable Dual-RNA-Guided DNA Endonuclease in Adaptive Bacterial Immunity. Science (80-.). 337, 816–821 (2012).
44. Metzger L & Iliakis G Kinetics of DNA Double-strand Break Repair Throughout the Cell Cycle as Assayed by Pulsed Field Gel Electrophoresis in CHO Cells. Int. J. Radiat. Biol 59, 1325–1339 (1991). [PubMed: 1677379]
45. Stenerlöw B, Karlsson KH, Cooper B & Rydberg B Measurement of prompt DNA double-strand breaks in mammalian cells without including heat-labile sites: results for cells deficient in nonhomologous end joining. Radiat. Res 159, 502–10 (2003). [PubMed: 12643795]
46. Wang M et al. PARP-1 and Ku compete for repair of DNA double strand breaks by distinct NHEJ pathways. Nucleic Acids Res. 34, 6170–6182 (2006). [PubMed: 17088286]

47. Kim S, Kim D, Cho SW, Kim J & Kim J-S Highly efficient RNA-guided genome editing in human cells via delivery of purified Cas9 ribonucleoproteins. Genome Res. 24, 1012–1019 (2014). [PubMed: 24696461]

48. Reid DA et al. Organization and dynamics of the nonhomologous end-joining machinery during DNA double-strand break repair. Proc. Natl. Acad. Sci 112, E2575–E2584 (2015). [PubMed: 25941401]

49. Bothmer A et al. Characterization of the interplay between DNA repair and CRISPR/Cas9-induced DNA lesions at an endogenous locus. (2017). doi:10.1038/ncomms13905

50. Ramirez RA, Lu J & Thomas KEH Quality of life for non-small cell lung cancer patients in the age of immunotherapy. Transl. Lung Cancer Res 7, S149–S152 (2018). [PubMed: 29782567]

Visual Overview

This figure summarizes the relationship of CRISPR/Cas gene editing complexes entering the cell, penetrating the nucleus and executing double-strand DNA breakage in the cell's genome. In panel A, we image nuclear entry, co-localization and exit of the RNP components by fluorescent microscopy. Quantification of this was carried out using fluorescence-activated cell sorting. The nucleus is stained blue (DAPI) while the two components of the CRISPR gene editing complex, the tracrRNA and the Cas9, are labeled with red (ATTO 550) and green (GFP) fluorescent tags respectively. The tracrRNA is the RNA binding section and the Cas9 protein is the nuclease that cleaves DNA. The red fluorescent RNA component localizes rapidly into the nucleus while the green fluorescent protein appears punctate at the nuclear membrane, merging or coalescing into the nucleus after four hours. Between one and eight hours, red fluorescence appears throughout the nucleus and cytoplasm, and after eight hours, both RNA and protein appear to exit the nucleus. At twenty-four hours, the green fluorescent protein is barely visible apart from the punctate remnants surrounding the nucleus and only small traces of red fluorescent RNA remain visible in the nucleus. After forty-eight hours, both fluorescent components are barely detectable and are thus believed to have either been destroyed or diluted within the cell milieu. In panel B, we present a graphical representation of the individual and dual fluorescence of CRISPR/Cas components, imaged in panel A, combined with the appearance of gene editing activity. We see two phases: Phase I encompasses RNP delivery and nuclear uptake, along with the initial signals of CRISPR-directed DNA cleavage of a single target site; phase II reveals elevated levels of indel formation likely through resection and repair of the target site after cleavage, along with the exit of the two fluorescent CRISPR/Cas components from the cell. Our data provide for the first time a visual snapshot of the timing of a CRISPR complex as it enters a tumor cell in relation to its DNA gene editing activity.

Implications

Our results begin to set a scientifically meritorious foundation for the exploitation of CRISPR-directed gene editing as an augmentative therapy for lung cancer and other solid tumors.

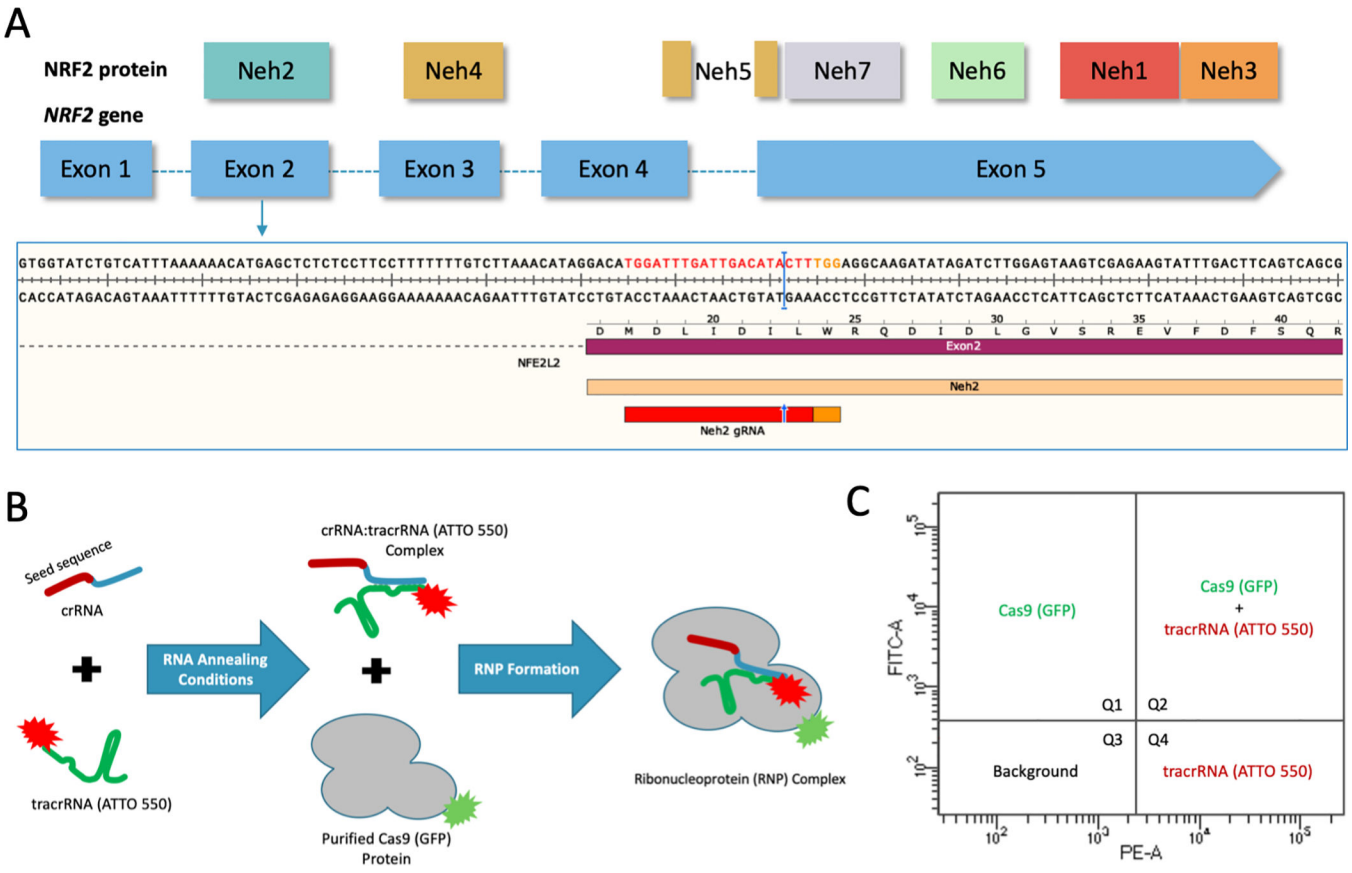

Figure 1.

(A) CRISPR design and *NRF2* sequence target. Structural domains of the NRF2 protein aligned to the exons of the *NRF2* gene. CRISPR/Cas9 was designed to target the beginning of exon 2 using the gRNA shown in red and the PAM sequence in orange with the cleavage site indicated by the blue arrow and bar. **(B)** CRISPR/Cas9 RNP assembly reaction using fluorescently labeled components. The crRNA contains the seed sequence (shown in red) designed to target exon 2 of the *NRF2* gene. The blue region of the crRNA is the interaction domain for annealing with tracrRNA (shown in green), which is labeled with the ATTO-550 dye. The crRNA and tracrRNA are annealed in equimolar concentrations. The Cas9 protein, which is labeled with GFP, is added for complete RNP formation. **(C)** FACS analysis of fluorescently labeled RNP components. An example of the localization of each fluorescent component on a FACS dot plot. Quadrant 1 (Q1) would contain cells with GFP fluorescence. Quadrant 2 (Q2) would contain cells with both GFP and ATTO 550 fluorescence. Quadrant 3 (Q3) would contain cells that do not exceed background fluorescence. Quadrant 4 (Q4) would contain cells with ATTO 550 fluorescence.

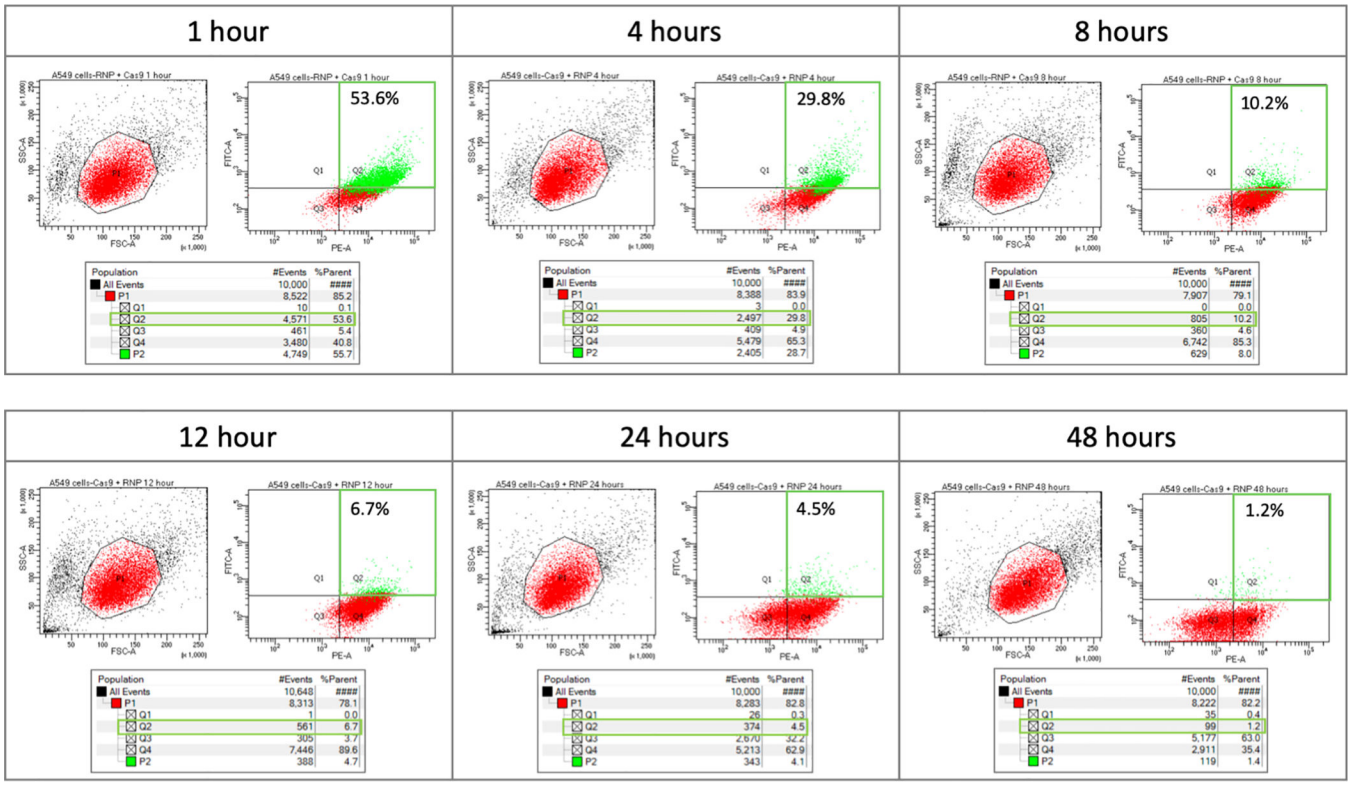

Figure 2.

Time course analysis of fluorescently labeled RNP using FACS. A549 cells were transfected with 20 pmol of fluorescently labeled RNP complex and analyzed via FACS to determine fluorescence intensity at 1, 4, 8, 12, 24, and 48 hours post nucleofection. The red area (P1) of the left hand graph contains the population of A549 cells that were further analyzed for fluorescence intensity. Quadrant 1 (Q1) would contain cells with GFP fluorescence. Quandrant 2 (Q2) would contain cells with both GFP and ATTO 550 fluorescence. Quadrant 3 (Q3) would contain cells that do not exceed background fluorescence. Quadrant 4 (Q4) would contain cells with ATTO 550 fluorescence. A549 cells with both fluorescently labeled RNP components – Cas (GFP) and tracrRNA (ATTO550), fall within quadrant 2 (outlined in green). Population 2 (P2), highlighted in green, was gated to capture GFP-positive cells that may have been omitted with standard gating. The table under each plot contains raw data for each quadrant.

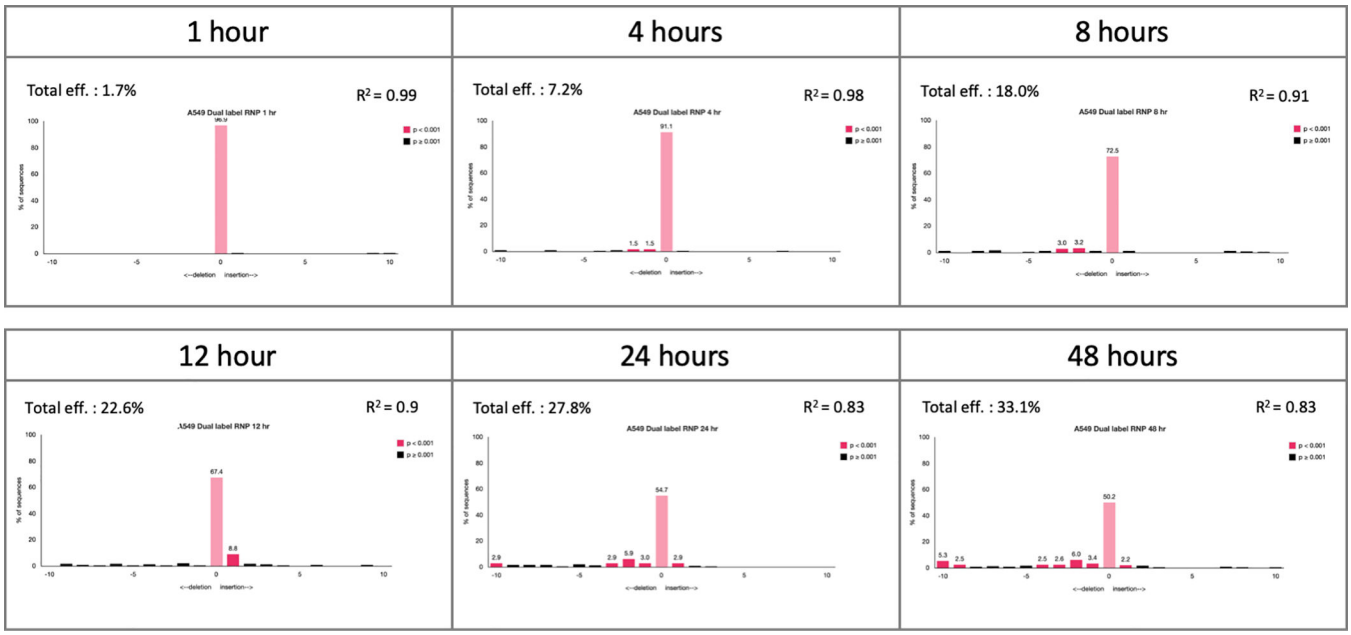

Figure 3.

Time course analysis of gene editing activity of fluorescently labeled RNP. The total, unsorted population of A549 cells transfected with 20 pmol of fluorescently labeled RNP complex was collected at each time point. Genomic DNA was isolated and the target region was PCR-amplified. The target region was then Sanger sequenced and analyzed for indel efficiency by TIDE.

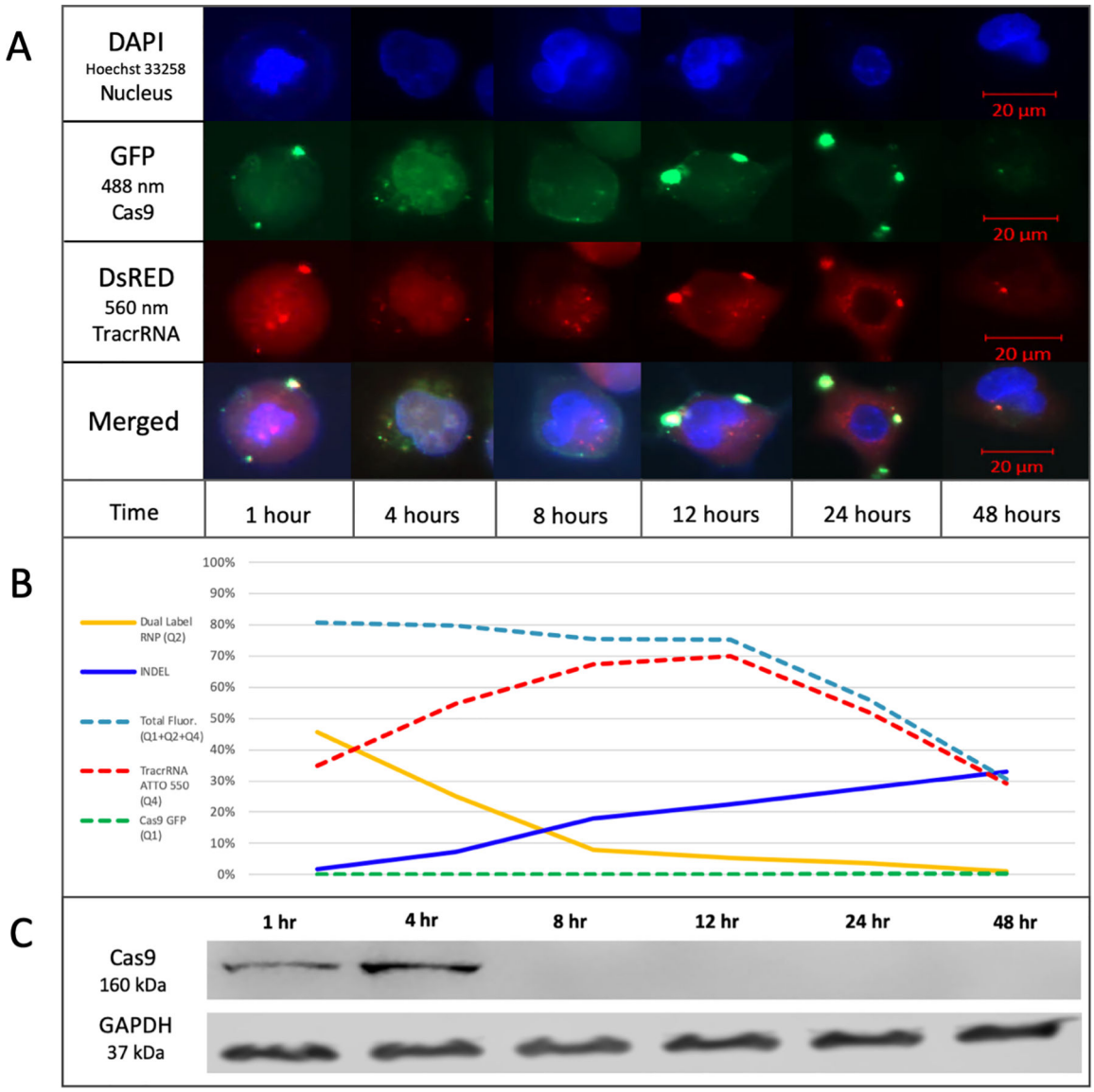

Figure 4.

(A) Time course analysis of the cellular localization of fluorescently labeled RNP. A549 cells were transfected with 20 pmol of fluorescently labeled RNP complex and seeded in 4-well chambers for imaging. Representative images of each time point are shown in the figure depicting localization of the fluorescently labeled RNP complex. The brightness of the images is enhanced to better visualize the localization of the RNP complex. Scale bar represents 20 µm. **(B)** Graphical representation of individual and dual fluorescence from FACS compared to indel formation. The graph displays the %Total of each quadrant at each time point. Dual Label RNP (Q2) represents each %Total from quadrant 2, which contains cells with both fluorescent components. INDEL represents each percentage for total indel efficiency by TIDE analysis of an unsorted bulk population transfected with the dual labeled RNP. Total Fluor (Q1+Q2+Q4) represents the sum of quadrant 1, 2, and 4 to assess the total population of cells with fluorescence. TracrRNA ATTO 550 (Q4) represents each %Total from quadrant 3, which contains cells with ATTO 550 fluorescence only. Cas9 GFP (Q1)

represents each %Total from quadrant 1, which contains cells with GFP fluorescence only. **(C)** Western blot analysis of Cas9 maintenance in cells. A549 cells were transfected with CRISPR/Cas9 RNP targeting exon 2 of *NRF2* and harvested at the indicated time points for western blot analysis using an antibody directed against spCas9. An antibody directed against GAPDH was used as the loading control.

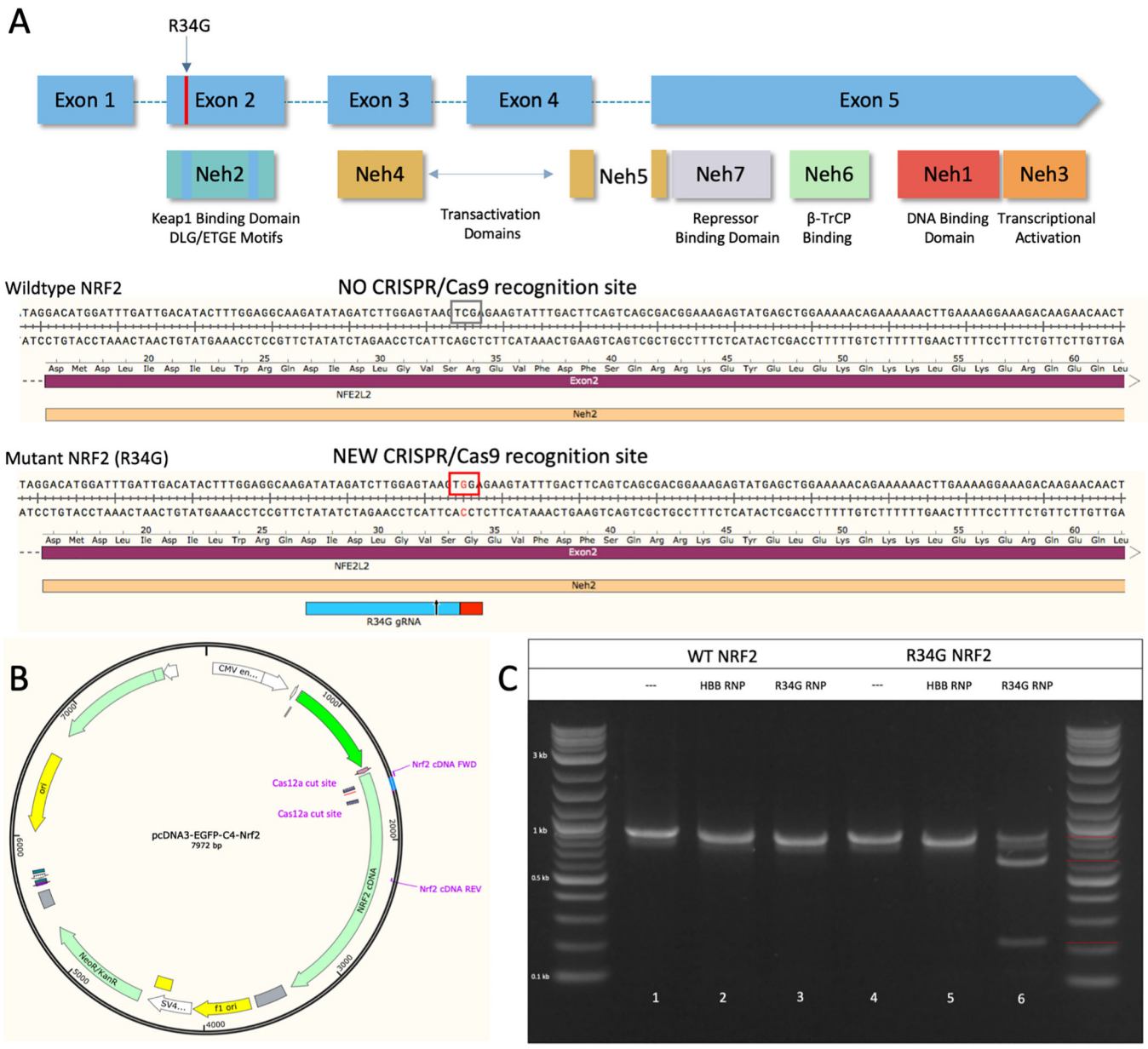

Figure 5.

(A) Structural domains and selective targeting of *NRF2*. The R34G mutation occurs in exon 2 of the *NRF2* gene, which encodes the Neh2 Domain of the NRF2 protein, shown in upper panel. The lower panel presents a schematic of the creation of a new CRISPR/Cas9 PAM site through the R34G mutation (TCG → TGG). **(B)** Recreation of the R34G mutation in a *NRF2* gene expression plasmid (pcDNA3-EGFP-C4-NRF2, Addgene). The *NRF2* expression plasmid was mutated to contain the R34G mutation using CRISPR-directed mutagenesis with two CRISPR/Cas12a cleavage sites and a duplexed oligonucleotide. **(C)** Proof-of-concept *in vitro* cleavage reaction using the R34G mutation as a CRISPR/Cas9 cleavage site. The *NRF2* expression plasmid was used to test the cleavage capacity of Cas9 with the new R34G mutation. Wildtype (WT NRF2) and mutated (R34G NRF2) *NRF2* expression plasmids were amplified and purified amplicons were used for cleavage

reactions. Reactions were visualized by gel electrophoresis. Lanes 1 and 5 are the *NRF2* amplicons incubated with buffer only (negative control). Lanes 2 and 5 are *NRF2* amplicons incubated with a nonspecific RNP (HBB RNP). Lanes 3 and 6 are NRF2 amplicons incubated with the R34G RNP. The red bars (right handside of ladder) indicate the size of uncut amplicons (901 bp) and cleavage products (222 & 679 bp).

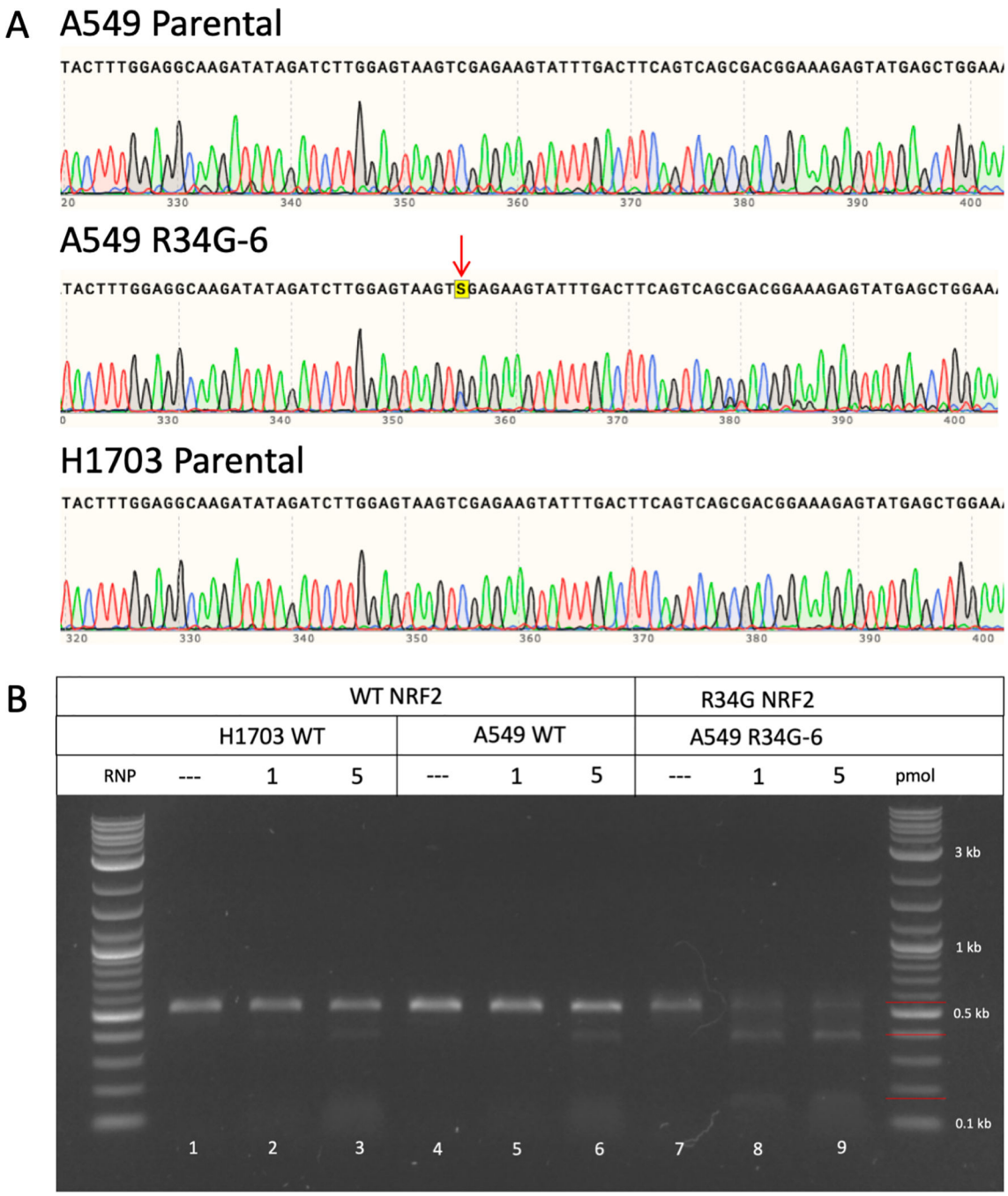

Figure 6.

(A) *NRF2* sequence analysis of A549 and H1703 parental cell lines and the A549 R34G-mutated cell line. Genomic DNA from each cell line was isolated and amplified across exon 2 of the *NRF2* gene. Amplicons were sanger sequenced and analyzed for mutations. A549 and H1703 parental cell lines contain a wildtype sequence; whereas the A549 R34G-6 clone contains a heterozygous R34G mutation, indicated by the red arrow. **(B)** *In vitro* cleavage reaction using wildtype and R34G-mutated *NRF2* amplicons with varying concentrations of R34G RNP. Genomic DNA was isolated from H1703 and A549 parental cell lines and the

A549 R34G-mutated cell line and amplified. Purified *NRF2* amplicons were incubated with 1 and 5 pmol of R34G RNP and the reactions were visualized by gel electrophoresis. Lanes 1, 4, and 7 are NRF2 amplicons incubated with buffer only (negative control). Lanes 2, 3 and 5, 6 are wildtype NRF2 amplicons incubated with R34G RNP. Lanes 8 and 9 are R34G mutated *NRF2* amplicons incubated with R34G RNP. The red bars (right handside of ladder) indicate the size of the uncut amplicons (530 bp) and cleavage products (145 & 385 bp).

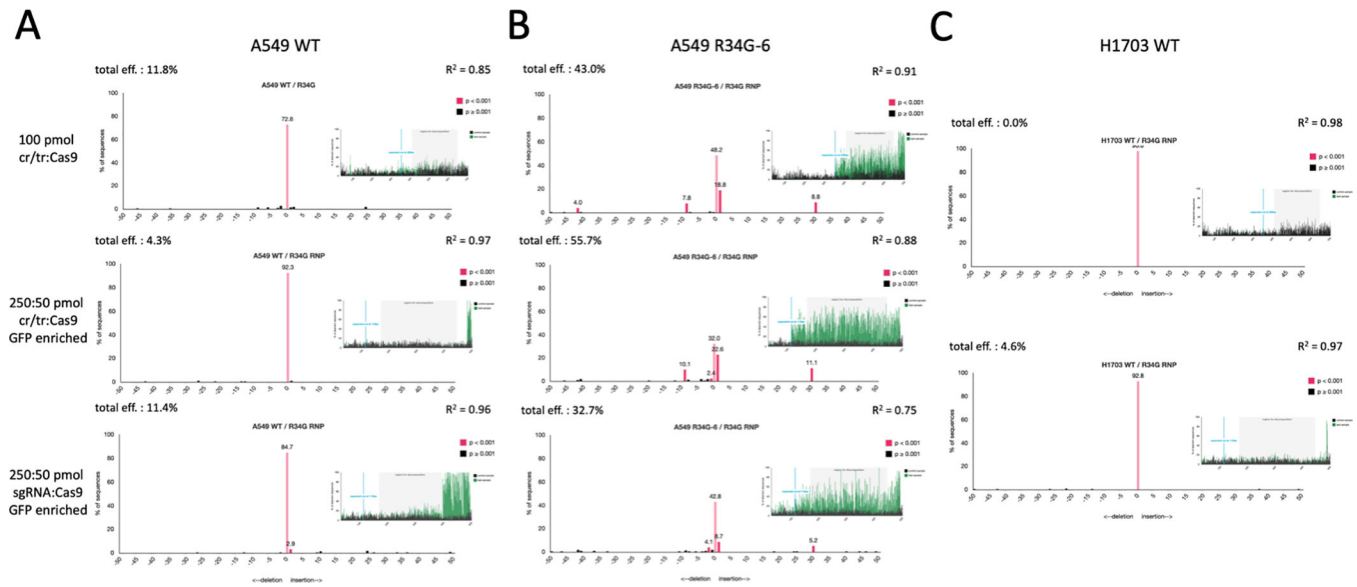

Figure 7.

Genetic analysis of the selective cleavage activity of the R34G-targeting RNP in a wildtype versus mutated *NRF2* sequence. This experiment was conducted using three different cell lines: **(A)** A549 parental cells, **(B)** A549 R34G-6 cells, **(C)** H1703 parental cells. Each cell line was transfected using three different conditions: 1) equimolar concentration of duplexed guide RNA to Cas9 (top panel); 2) five times the amount of duplexed guide RNA to Cas9 (middle panel); 3) five times the amount of single guide RNA to Cas9 (bottom panel). Gene editing activity was assessed by bulk sequence analysis using TIDE. Each panel represents the data output of indel formation from TIDE.